



**University of  
Zurich**<sup>UZH</sup>

**Zurich Open Repository and  
Archive**

University of Zurich  
University Library  
Strickhofstrasse 39  
CH-8057 Zurich  
[www.zora.uzh.ch](http://www.zora.uzh.ch)

---

Year: 2023

---

## **Mapping the myelin bilayer with short-T<sub>2</sub> MRI: Methods validation and reference data for healthy human brain**

Baadsvik, Emily Louise ; Weiger, Markus ; Froidevaux, Romain ; Faigle, Wolfgang ; Ineichen, Benjamin Victor ; Pruessmann, Klaas Paul

DOI: <https://doi.org/10.1002/mrm.29481>

Posted at the Zurich Open Repository and Archive, University of Zurich

ZORA URL: <https://doi.org/10.5167/uzh-253572>

Journal Article

Published Version



The following work is licensed under a Creative Commons: Attribution-NonCommercial 4.0 International (CC BY-NC 4.0) License.

Originally published at:

Baadsvik, Emily Louise; Weiger, Markus; Froidevaux, Romain; Faigle, Wolfgang; Ineichen, Benjamin Victor; Pruessmann, Klaas Paul (2023). Mapping the myelin bilayer with short-T<sub>2</sub> MRI: Methods validation and reference data for healthy human brain. *Magnetic Resonance in Medicine*, 89(2):665-677.

DOI: <https://doi.org/10.1002/mrm.29481>

# Mapping the myelin bilayer with short-T<sub>2</sub> MRI: Methods validation and reference data for healthy human brain

Emily Louise Baadsvik<sup>1</sup>  | Markus Weiger<sup>1</sup> | Romain Froidevaux<sup>1</sup>  | Wolfgang Faigle<sup>2</sup> | Benjamin Victor Ineichen<sup>3</sup> | Klaas Paul Pruessmann<sup>1</sup> 

<sup>1</sup>Institute for Biomedical Engineering, ETH Zurich and University of Zurich, Zurich, Switzerland

<sup>2</sup>Neuroimmunology and MS Research Section, Neurology Clinic, University of Zurich, University Hospital Zurich, Zurich, Switzerland

<sup>3</sup>Department of Neuroradiology, Clinical Neuroscience Center, University Hospital Zurich, University of Zurich, Zurich, Switzerland

## Correspondence

Markus Weiger, Institute for Biomedical Engineering, ETH Zurich and University of Zurich, Gloriastrasse 35, 8092, Zurich, Switzerland.

Email: [weiger@biomed.ee.ethz.ch](mailto:weiger@biomed.ee.ethz.ch)

**Purpose:** To explore the properties of short-T<sub>2</sub> signals in human brain, investigate the impact of various experimental procedures on these properties, and evaluate the performance of three-component analysis.

**Methods:** Eight samples of non-pathological human brain tissue were subjected to different combinations of experimental procedures including D<sub>2</sub>O exchange and frozen storage. Short-T<sub>2</sub> imaging techniques were employed to acquire multi-TE (33–2067 μs) data, to which a three-component complex model was fitted in two steps to recover the properties of the underlying signal components and produce amplitude maps of each component. For validation of the component amplitude maps, the samples underwent immunohistochemical myelin staining.

**Results:** The signal component representing the myelin bilayer exhibited super-exponential decay with T<sub>2,min</sub> of 5.48 μs and a chemical shift of 1.07 ppm, and its amplitude could be successfully mapped in both white and gray matter in all samples. These myelin maps corresponded well to myelin-stained tissue sections. Gray matter signals exhibited somewhat different components than white matter signals, but both tissue types were well represented by the signal model. Frozen tissue storage did not alter the signal components but influenced component amplitudes. D<sub>2</sub>O exchange was necessary to characterize the non-aqueous signal components, but component amplitude mapping could be reliably performed also in the presence of H<sub>2</sub>O signals.

**Conclusions:** The myelin mapping approach explored here produced reasonable and stable results for all samples. The extensive tissue and methodological investigations performed in this work form a basis for signal interpretation in future studies both *ex vivo* and *in vivo*.

## KEYWORDS

high-performance gradient, super-Lorentzian lineshape, tissue characterization, tissue preparation, ultrashort TE, white and gray matter

## 1 | INTRODUCTION

The central nervous system (CNS) relies heavily on myelin for efficient signal transmission along neural pathways.<sup>1,2</sup> Damage to the myelin sheath is an integral feature of several neuroinflammatory diseases such as multiple sclerosis and can result in severe disability.<sup>3,4</sup> The ability to non-invasively map myelin content is highly desirable for monitoring of demyelinating disorders, pathomechanistic studies on demyelination and myelin repair, and development of putative remyelinating drug candidates.

CNS myelin is a compacted extension of the plasma membrane of oligodendrocytes. The membrane wraps concentrically around axons, trapping layers of intra- and extracellular water in the process,<sup>5</sup> and develops a characteristic lipid (70% of dry mass) and protein composition.<sup>2,6</sup> Consequently, the myelin sheath has two primary constituents: the trapped water collectively referred to as myelin water and the lipid-protein bilayer.

CNS myelin is primarily present in white matter (WM), in which it comprises approximately 50% of dry mass, but oligodendrocytes and myelin-wrapped axons exist also in gray matter (GM).<sup>2</sup>

MRI lends itself well to myelin mapping due to its safe, non-invasive application and its rich capacity for probing tissue properties. The majority of research toward myelin mapping with MRI is based on the analysis of signals stemming from aqueous protons,<sup>7</sup> for which myelin sensitivity is achieved either through the distinct relaxation properties of myelin water<sup>8</sup> or through interactions between non-aqueous and aqueous magnetization pools.<sup>9</sup> Many techniques exploiting aqueous signals are readily available for use *in vivo* and have been shown to correlate with histological myelin stains and provide sensitivity to various CNS disorders.<sup>5,10,11</sup> These techniques represent a notable advancement in myelin specificity compared to conventional MRI, but yield inherently rather indirect measures of myelin content.

More direct myelin bilayer imaging methods are warranted to complement or possibly outperform the techniques relying on aqueous signals, but targeting signals from protons in the myelin bilayer has traditionally been impractical. Aqueous signals, with  $T_2$ s in the range of tens to hundreds of milliseconds, are straightforward to capture with standard MRI systems. In contrast, due to the specific configuration of the myelin sheath, signals from bilayer-bound protons exhibit a  $T_2$  spectrum ranging from a few microseconds to tens of milliseconds,<sup>12</sup> with around 75% of the signals exhibiting  $T_2$ s below 100  $\mu$ s.<sup>13</sup>

As reviewed by Weiger et al.,<sup>14</sup> research in recent years has demonstrated that dedicated short- $T_2$  imaging

technology is capable of capturing and spatially resolving rapidly decaying signals from different tissues and materials, particularly for decay constants down to the hundreds of microseconds range. Using custom-built, high-performance RF and gradient hardware, even signals with ultrashort decay constants down to 10  $\mu$ s have been imaged at high resolution.<sup>15</sup> Several studies have proposed the use of short- $T_2$  techniques for imaging of the myelin bilayer,<sup>12,16–25</sup> and a pilot myelin study using the imaging system described by Froidevaux et al.<sup>15</sup> demonstrated clear acquisition-related advantages afforded by the advanced hardware.<sup>13</sup>

Most reports of myelin bilayer imaging are based on *ex vivo* studies with large variations between experimental approaches. As such, it is yet unclear how best to interpret resulting data and whether the same interpretations would apply also to *in vivo* signals.

Much of the uncertainty in data interpretation relates to the selection, storage and preparation of imaging samples. Experimental approaches to myelin bilayer signal examination frequently involve the use of animal<sup>12,13,21–23,26,27</sup> or human<sup>17,19,20</sup> tissue samples, and it is common practice to freeze the tissue between dissection and imaging. However, it is unclear how well the signal properties of animal tissue match those of human tissue and whether freezing alters the MR signals like formalin fixation has been shown to do.<sup>20</sup> In addition, background water signals are often reduced by  $D_2O$  exchange in order to isolate the contributions from non-aqueous signals such as those stemming from the myelin bilayer.<sup>12,13,19–23,26</sup> Such chemical preparation is not feasible *in vivo*, and while an initial attempt showed promising results for myelin bilayer mapping also in non-exchanged tissue,<sup>13</sup> key questions remain regarding which signal analysis approaches are valid in the presence of dominant background signals.

In this work, MRI signals from non-aqueous and aqueous protons in non-pathological human brain tissue (WM and GM) are observed and assigned to three signal components. The results are compared with literature findings in animal samples to explore the validity of animal tissue as a substitute for human tissue in MR-based myelin research. Furthermore, the effects of frozen sample storage on the MRI signals are investigated. The performance of the three-component analysis approach is discussed, with focus on the differences between employment in  $D_2O$ -exchanged samples and non-exchanged counterparts. Finally, amplitude maps of the signal components are produced and qualitatively compared with myelin-stained tissue sections, high-resolution ultrashort- $T_2$  reference images and photographs of the samples.

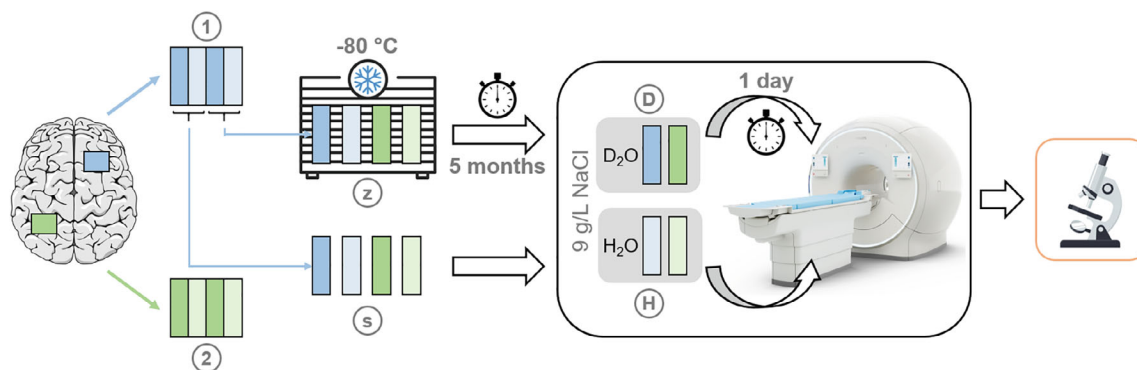


**FIGURE 1** Schematic showing the processing steps for each sample. Tissue blocks from two regions (“1” and “2”) on the cerebrum were divided into four samples each, half of which were imaged directly and half of which were stored at  $-80^{\circ}\text{C}$  for five months prior to imaging. Of the four samples that were arranged either fresh (“s”) or frozen–thawed (“z”), one from each tissue block underwent a 24-h, two-step  $\text{D}_2\text{O}$  exchange (“D”) while the other was placed in  $\text{H}_2\text{O}$  (“H”). After imaging, the samples were processed for myelin immunohistochemistry. Note that the placement of the tissue blocks on the cerebrum are for demonstration purposes only and are not meant to indicate the anatomical locations of the dissected tissue

## 2 | METHODS

### 2.1 | Tissue samples

Two tissue blocks from different regions of the cerebrum of a 56-year-old male donor were excised at autopsy (post-mortem interval: six hour). The patient died of a cardiovascular event, and neuropathological workup did not suggest gross brain pathology. Written informed consent was obtained, and the study was approved by the regional ethics review board.

Each of the tissue blocks (labeled “1” and “2”, extracted from the temporal and frontal lobes, respectively) was divided into four samples on average  $5 \times 25 \times 18 \text{ mm}^3$ . Two neighboring samples were imaged promptly after autopsy (referred to as fresh samples, labeled “s”), and the remaining two neighboring samples were stored at  $-80^{\circ}\text{C}$  for five months prior to thawing and subsequent imaging (referred to as frozen samples, labeled “z”). For each set of two samples, one was subjected to  $\text{D}_2\text{O}$  exchange (referred to as  $\text{D}_2\text{O}$  samples, labeled “D”) performed in two steps over a total of 24 h (based on the procedures described by Wilhelm et al.<sup>12</sup> and Weiger et al.<sup>13</sup>). The samples not subjected to  $\text{D}_2\text{O}$  exchange were placed in water (referred to as  $\text{H}_2\text{O}$  samples, labeled “H”) to avoid dehydration and imaged directly. Both the  $\text{D}_2\text{O}$  and  $\text{H}_2\text{O}$  solutions were saline (9 g/L NaCl). Samples were stored at  $5^{\circ}\text{C}$  while awaiting imaging, and all imaging was performed with the samples at room temperature. A schematic of the full procedure is provided in Figure 1.

### 2.2 | Data acquisition

In order to capture the rapidly decaying signals from the myelin bilayer, dedicated ultrashort- $T_2$  techniques

and hardware were employed. A 3 T Philips Achieva (Philips Healthcare, the Netherlands) system was equipped with a high-performance gradient insert<sup>28</sup> capable of gradient strength in excess of 200 mT/m at 100% duty cycle, and the acquisition system was bypassed by a dedicated RF chain<sup>29</sup> including fast transmit/receive switches.<sup>30</sup> A  $^1\text{H}$ -free loop coil of 40 mm diameter was used for both transmit and receive operations.

Two 3D imaging protocols were applied. The first protocol utilized single-point imaging (SPI)<sup>31</sup> to acquire 14 images at TE between 33 and 2067  $\mu\text{s}$ , which were used for model fitting. SPI captures the full k-space at time TE, enabling unbiased voxel-wise analysis because, with no time evolution across k-space, each image accurately reflects the signal state at the respective TE. With the maximum gradient strength of 221 mT/m employed at the shortest TE, the nominal isotropic resolution was limited to 1.56 mm. The second protocol utilized zero-TE imaging with hybrid filling of the dead-time gap (HYFI)<sup>32</sup> to acquire a high-resolution (0.39 mm isotropic) ultrashort- $T_2$  reference image. Further details on the protocols can be found in Table 1.

### 2.3 | Data analysis

The data analysis procedure consisted of three steps: (1) determining a signal model that approximates true tissue composition and facilitates constructive analysis; (2) evaluating the parameters of the signal components to gain knowledge of the underlying tissue and reduce the unknowns in the signal model; and (3) establishing a procedure for myelin mapping based on the formulated signal model.

TABLE 1 Protocols for MRI of the myelin bilayer

Protocol	FOV [mm]	$\Delta r$ [mm]	BW [kHz]	TE [ $\mu$ s]	RF pulse	TR [ms]	NSA	Scan time [m:s]	HYFI-A	HYFI-T <sub>2</sub> [ $\mu$ s]
SPI	50	1.56	7.5–470	2067–33	2 $\mu$ s hard	3	4	03:34	N/A	N/A
HYFI	50	0.39	425	12	2 $\mu$ s hard	1	32	27:41	0.17	50

Note: The first protocol uses an SPI<sup>31</sup> sequence with spherical k-space support to acquire a multi-TE image series. The second protocol uses a HYFI<sup>32</sup> sequence to acquire a high-resolution ultrashort-T<sub>2</sub> reference image. Pulse power was adjusted for maximum steady-state signal, calibrated in a D<sub>2</sub>O sample to specifically optimize non-aqueous signals. The flip angles of approximately a few degrees were adjusted for the two protocols according to their different TRs to yield equivalent contrast. The scan time stated for the SPI protocol is per image, and the full multi-TE series consisted of 14 images.

Abbreviations: BW, image bandwidth; HYFI-A, HYFI amplitude coefficient; HYFI-T<sub>2</sub>, HYFI target T<sub>2</sub>; NSA, number of signal averages;  $\Delta r$ , nominal 3D isotropic resolution.

### 2.3.1 | Signal model

A three-component signal model was employed, which splits the non-aqueous signals into an ultrashort (U) and a short (S) component, both of super-Lorentzian lineshape,<sup>33,34</sup> and represents the aqueous signals by one component (W) of Lorentzian lineshape. Following the interpretation by Weiger et al.<sup>13</sup> (for WM), the U-component represents the myelin bilayer and the S-component represents residual non-aqueous content.

The signal evolution under this model is described by

$$S_{\text{voxel}}(t) = e^{i(\varphi + \Delta\omega t)} \left[ A_U D_{\text{SL}}(T_{2,\text{min},U}, t) e^{i\delta_U \omega_0 t} + A_S D_{\text{SL}}(T_{2,\text{min},S}, t) e^{i\delta_S \omega_0 t} + A_W D_L(T_{2,W}, t) e^{i\delta_W \omega_0 t} \right],$$

where  $\varphi$  is an arbitrary global phase,  $\Delta\omega$  is a local resonance offset and  $\omega_0$  is the <sup>1</sup>H Larmor frequency.  $A_n$ ,  $\delta_n$  and  $T_{2,n}$  or  $T_{2,\text{min},n}$  are the amplitude, chemical shift and decay constant of component  $n$ , respectively, where  $T_2$  characterizes the Lorentzian lineshape of decay function  $D_L$  and  $T_{2,\text{min}}$  characterizes the super-Lorentzian lineshape of decay function  $D_{\text{SL}}$ . The full form of the decay functions  $D_L$  and  $D_{\text{SL}}$  are provided in Supporting Information Part 1.

A two-component model with only one component representing the non-aqueous signals was also explored. Unless otherwise stated, the three-component model was used.

Note that decay constants as a tissue property are denoted by  $T_2$ , while any measured signals technically decay by  $T_2^*$ . However,  $T_2'$  is considered negligible here, and, therefore, the decay constants resulting from signal analysis retain the notation used to define the signal model.

Because water signals have decayed almost negligibly after the longest TE of the SPI series, the decay constant of the W-component could not be reliably fitted and was instead fixed at 50 ms for all analyses: although water in the brain exhibits a range of decay constants, the exact value used to characterize the W-component is

of little practical impact in this study. Also the chemical shift of the W-component was fixed (at 4.7 ppm) and was used to calibrate the chemical shifts of the non-aqueous components.

### 2.3.2 | Component analysis: open fits

To determine the parameter values of the signal model, least-squares fitting was employed. For details on the algorithm, please consult the published analysis code (see Data Availability Statement). All parameters of the signal model – except those fixed for the W-component – were treated as unknowns, and the bounds on the parameters were kept wide to avoid making assumptions on the underlying components; we refer to such fits as open fits.

Open fits were performed on complex signal values averaged over large regions of WM or GM, which stabilized the fitting with respect to noise and potential local signal variations. The regions were chosen based on tissue anatomy seen in the high-resolution reference images, and were generally as large as possible while excluding voxels at tissue boundaries to limit partial volume effects. Such signal averaging is valid as long as variations in local resonance offset are small. Any mention of WM or GM regions or averaged signals for a given sample refers to the same data.

### 2.3.3 | Myelin mapping: fixed fits

Applying the fitting procedure from analysis step 2 on a single-voxel basis would yield maps of each free model parameter. With the interpretation that the U-component represents the myelin bilayer, a map of the amplitude of the U-component is a myelin map.

In order to enable useful interpretation, the amplitudes in the myelin map must be comparable between voxels, which can be achieved by defining the same signal components in each voxel (see the Discussion section). Reasonable component decay constants and chemical shifts were



therefore determined from the open fits and fixed in the voxel-wise fits. We refer to fits with fixed component decay constants and chemical shifts as fixed fits. Unless otherwise stated, the component parameters used in the fixed fits were the mean values found in WM; fixed fits based on the mean values found in GM were also explored.

Fixed fits were also run on the averaged WM and GM signals in order to compare component amplitudes in the two tissue types and across samples subjected to different experimental procedures. The absolute component amplitudes found for different datasets are not directly comparable due to variations in experimental factors such as coil loading and coil sensitivity. Therefore, amplitude normalization was performed, using different procedures for the aqueous and non-aqueous components: the aqueous component amplitude was normalized by the sum of all component amplitudes, while the non-aqueous component amplitudes were normalized by the sum of non-aqueous component amplitudes to quantify their relative contributions to the rapidly decaying signals.

## 2.4 | Processing

Tricubic interpolation was performed on all SPI data prior to analysis, reducing voxel size by a factor of two in each dimension. An additional in-plane interpolation by a factor of three was applied to all MRI-based images for display purposes.

Amplitude maps of the non-aqueous components in H<sub>2</sub>O samples were masked based on the sample outline in the respective W-component amplitude map.

For H<sub>2</sub>O samples, the two longest-TE data points were discarded for fitting (i.e.,  $TE_{\max, H_2O} = 827 \mu s$ ) because they exhibited unstable behavior, an effect that was not detected in D<sub>2</sub>O samples and is possibly related to the longer lifetime or larger presence of water signals. A linear fit to the phase of the remaining two longest-TE data points was used to determine an approximate value for the local resonance offset in H<sub>2</sub>O datasets, which was corrected out of the data for WM and GM region fits. Using this correction avoids the assumption that the local resonance offset is equal for all voxels included in signal averages and ensures that the local resonance offset parameter stays well within fit boundaries. This correction is not valid for D<sub>2</sub>O data because the water component does not sufficiently dominate the longest-TE data points.

## 2.5 | Histological staining

After imaging, the brain samples were snap frozen at  $-80^\circ C$  and subsequently cryosectioned into  $20 \mu m$

thick sections. The sections underwent immunohistochemistry for myelin oligodendrocyte glycoprotein (MOG, primary antibody concentration 1:50), which is a key myelin component. For a complete overview of the histological processing, see Supporting Information Part 2.

## 3 | RESULTS

The magnitude and phase behavior of the averaged WM signals for samples subjected to different experimental procedures (tissue block 1) are displayed in Figure 2. For the fresh D<sub>2</sub>O sample, the GM region is also included. H<sub>2</sub>O-sample magnitudes converge to a higher level than D<sub>2</sub>O-sample magnitudes, reflecting background water levels, and the phase curve shows characteristic behavior for D<sub>2</sub>O samples while for H<sub>2</sub>O samples the linear water phase dominates. Fresh samples exhibit a consistently higher magnitude than frozen samples, but the overall behavior is similar.

The decay constants and chemical shifts of the non-aqueous components found by the open fits are given in Table 2 for the WM and GM regions in all D<sub>2</sub>O samples. There is a clear range of decay constant for each component: in WM, the U-component averages  $5.48 \mu s$  and the S-component averages  $102 \mu s$ , and in GM these values are prolonged to  $9.42 \mu s$  and  $171 \mu s$ , respectively. The chemical shifts are also quite consistent, averaging  $1.07 \text{ ppm}$  for the U-component and  $2.09 \text{ ppm}$  for the S-component in WM, and  $0.58 \text{ ppm}$  for the U-component and  $2.39 \text{ ppm}$  for the S-component in GM.

Figure 3 shows a series of comparison plots of magnitude (top row) and phase (bottom row) behavior for different fits in the frozen D<sub>2</sub>O sample from tissue block 1. Note that the axis ranges are set individually for each plot. In Figure 3A, an open fit using the default three-component signal model is compared with an open fit using the two-component signal model, and it is clear that the two-component model does not adequately represent the signal behavior, whereas the three-component model fits the data well. Figure 3B illustrates the similarities between open and fixed fits to averaged WM signals, and the phase plot highlights the noise variations at low TE. Similarly, Figure 3C displays open and fixed fits to averaged GM signals, and, in addition, a fixed fit based on the average signal components found in GM is included. While there are differences between the components found by the open fits and the components used for the fixed fits (see Table 2), the differences in fit performance are marginal throughout Figure 3B–D. Figure 3D emphasizes the differences between WM and GM signal behavior. Overall, the presented details illustrate the suitability of the employed

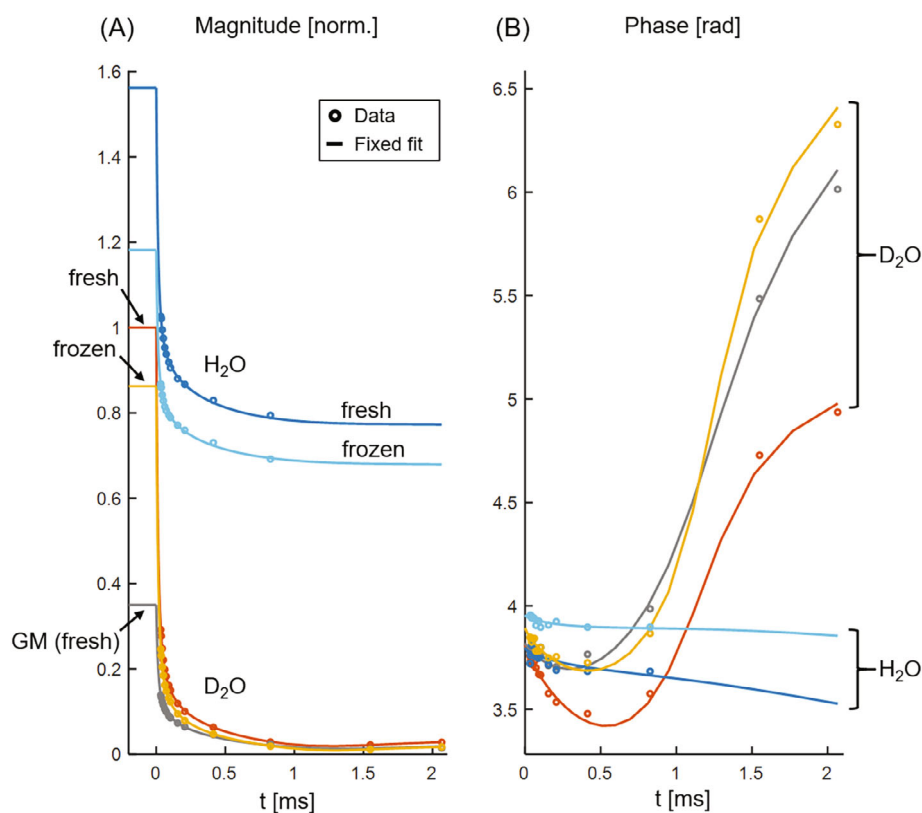


**FIGURE 2** Magnitude (A) and phase (B) of the SPI data and associated fixed fits for the samples from tissue block 1. Data points represent an average over large WM regions unless specified as GM data. The magnitudes are normalized by the fit magnitude at time zero in WM for the fresh D<sub>2</sub>O sample. H<sub>2</sub>O and D<sub>2</sub>O samples are clearly distinguishable in both plots. In the absence of a dominant water pool, the phase curves exhibit a characteristic shape; in contrast, the phase of the H<sub>2</sub>O data is approximately linear and, because the local resonance offset has been corrected for, relatively flat. Frozen samples have reduced magnitude with respect to their fresh counterparts but otherwise exhibit similar signal behavior. The GM region has significantly lower magnitude than the WM region from the same sample, but the general signal behavior of the two tissue types is comparable

**TABLE 2** Non-aqueous component parameters  $T_{2,\min}$  and chemical shift ( $\delta$ ) found by open fits to averaged WM and GM signals for all D<sub>2</sub>O (“D”) samples, as well as mean value and SD per tissue type

	Sample	$T_{2,\min,U}$ [ $\mu$ s]		$T_{2,\min,S}$ [ $\mu$ s]		$\delta_U$ [ppm]		$\delta_S$ [ppm]	
WM	1Ds	6.76	(0.16)	92.1	(0.74)	1.02	(0.02)	2.10	(0.01)
	2Ds	4.94	(0.06)	122	(0.46)	0.85	(0.01)	1.96	(0.00)
	1Dz	5.53	(0.16)	88.1	(0.48)	1.30	(0.02)	2.06	(0.01)
	2Dz	4.71	(0.11)	108	(0.51)	1.10	(0.01)	2.25	(0.00)
	Mean	5.48		102		1.07		2.09	
	SD	0.92		15.5		0.18		0.12	
GM	1Ds	10.3	(0.19)	157	(1.28)	0.77	(0.02)	2.47	(0.00)
	2Ds	8.88	(0.08)	219	(1.07)	0.10	(0.01)	2.20	(0.00)
	1Dz	10.6	(0.49)	152	(3.88)	0.69	(0.05)	2.35	(0.01)
	2Dz	7.92	(0.34)	155	(2.35)	0.75	(0.04)	2.51	(0.01)
	Mean	9.42		171		0.58		2.39	
	SD	1.25		32.2		0.32		0.14	

*Note:* Standard errors obtained by propagation of the noise variance in the underlying images are given in parenthesis.  $T_{2,\min}$  is longer in GM than WM, but the signal components each exhibit a clear range of decay constant irrespective of tissue type. In WM and partly in GM, there is more variation between the two tissue blocks (“1” and “2”) than between fresh (“s”) and frozen (“z”) samples. This indicates that anatomical location affects the detectable signal components to some degree while freezing has little impact. The GM components found in sample 2Ds deviate somewhat from those found in the other samples, which is considered to be a manifestation of instability in the open fits. GM fits are generally less stable than WM fits due to the lower signal level.

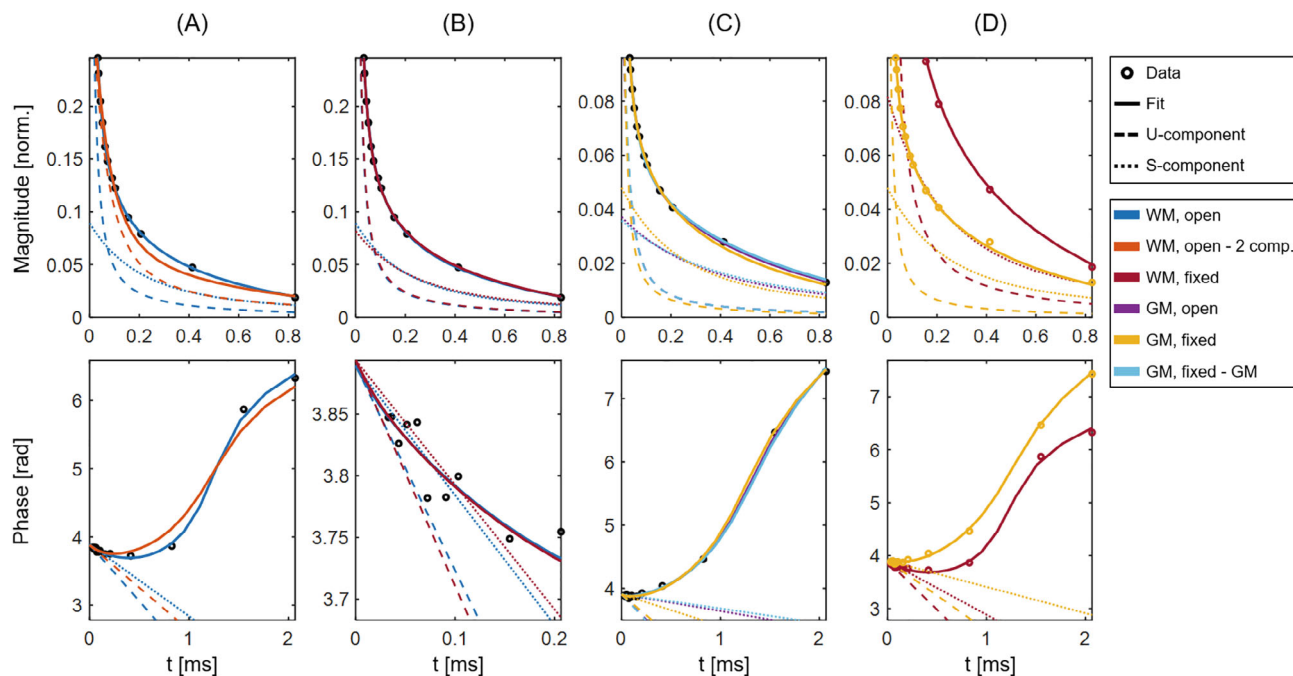


**FIGURE 3** Comparison plots of magnitude (top row, same normalization as applied in Figure 2) and phase (bottom row) for different fits to averaged WM and GM signals in a representative sample (the frozen D<sub>2</sub>O sample from tissue block 1). Note the different axes used for the different plots. The underlying data points are shown as black circles in cases in which all fits are based on the same data, and as colored circles in cases in which the fits are based on different data. The W-component is not shown for simplicity, but would manifest as a near-horizontal line. A, Open fits in WM using both three-component (blue) and two-component (orange) signal models. B, Open (blue) and fixed (maroon) fits in WM. C, Open (purple) and fixed (yellow) fits in GM, as well as an additional fixed fit (light blue) based on the average signal components found in GM (see Table 2). D, Fixed fits in WM (maroon) and GM (yellow), highlighting the differences in signal behavior

three-component model and the use of fixed fits with equal component parameters for WM and GM.

Fixed fits applied to several averaged WM and GM signals are displayed in Figure 2, and normalized component amplitudes obtained from such fits for all samples are given in Table 3. The normalized W-component amplitudes in D<sub>2</sub>O samples reflect the extent of D<sub>2</sub>O exchange and thus should not be directly compared, but comparing W-component amplitudes within the same sample shows roughly twice as high a water fraction in GM as in WM. For H<sub>2</sub>O samples, the GM water increase averages around 30%. Both observations primarily reflect lower content of non-aqueous components in GM than in WM. The normalized W-component amplitudes in H<sub>2</sub>O samples are slightly lower than the brain water content expected from literature (approximately 70% in WM and 80% in GM)<sup>35</sup>; although we urge caution when interpreting fitted component amplitudes (see the Discussion section), this apparent water reduction is likely a consequence of T<sub>1</sub> weighting in the underlying data (see Supporting Information Part 3). In WM, the amplitude ratio between the non-aqueous components  $A_U/A_S$  is roughly 90/10, except for the frozen H<sub>2</sub>O samples for which the ratio is rather 80/20. In GM, the  $A_U/A_S$  ratio is generally around 80/20, with deviations for samples 2Ds and 2Hs, which are closer to a 95/5

ratio, and the frozen H<sub>2</sub>O samples, for which the ratio is around 70/30. Differences between fresh and frozen H<sub>2</sub>O samples are also present in the W-component, for which the amplitude is slightly higher for frozen than fresh samples.

Amplitude maps of the three signal components, obtained by performing voxel-wise fixed fits, are displayed for all samples in Figures 4 (tissue block 1) and 5 (tissue block 2) along with photographs, myelin-stained tissue sections, and high-resolution reference images. Overall, good correspondence is seen between all image types (see for instance sample 1Dz in Figure 4), but due to the thickness and pliability of the samples and the resolution of the component amplitude maps, some topological sample features vary slightly between photographs, MRI slices and/or stained sections. Some of the component amplitude maps also suffer from partial volume effects. Certain myelin-stained sections exhibit only weak WM/GM contrast, which likely relates to variability in the staining process. The similarities between U-component amplitude maps and MOG staining density are of particular interest because they strengthen the interpretation of the U-component as representing the myelin bilayer. The W-component amplitude maps convincingly reflect water content, accounting for the T<sub>1</sub> weighting in the



**TABLE 3** Normalized amplitudes for each signal component in WM and GM regions for all samples, determined from fits in which the component decay constants and chemical shifts were fixed at the average WM values given in Table 2

	Sample	$\frac{A_W}{A_W+A_U+A_S}$	$\frac{A_U}{A_U+A_S}$	$\frac{A_S}{A_U+A_S}$
WM	1Ds	0.03	0.90	0.10
	2Ds	0.03	0.93	0.07
	1Dz	0.02	0.90	0.10
	2Dz	0.05	0.90	0.10
	1Hs	0.52	0.87	0.13
	2Hs	0.47	0.94	0.06
	1Hz	0.60	0.81	0.19
	2Hz	0.58	0.81	0.19
	Mean	0.54 <sup>a</sup>	0.88	0.12
	SD	0.06 <sup>a</sup>	0.05	0.05
GM	1Ds	0.06	0.77	0.23
	2Ds	0.06	0.93	0.07
	1Dz	0.04	0.81	0.19
	2Dz	0.09	0.81	0.19
	1Hs	0.71	0.75	0.25
	2Hs	0.61	0.96	0.04
	1Hz	0.76	0.73	0.27
	2Hz	0.75	0.70	0.30
	Mean	0.71 <sup>a</sup>	0.81	0.19
	SD	0.07 <sup>a</sup>	0.09	0.09

*Note:* Standard errors are on the order of  $10^{-3}$ – $10^{-5}$ . The mean value and SD for each tissue type are also provided, which for the normalized W-component amplitudes were determined only over the H<sub>2</sub>O samples. Relative water content is much higher in H<sub>2</sub>O samples (“H”) than in D<sub>2</sub>O samples (“D”) and higher in GM than in WM. The amplitude distribution of non-aqueous signals  $A_U/A_S$  is around 90/10 in WM and 80/20 in GM. Frozen tissue (“z”) differs notably from fresh tissue (“s”) in H<sub>2</sub>O samples: in the frozen samples, the normalized amplitude of the W-component is higher and the  $A_U/A_S$  ratio tends toward a lower U-component contribution (80/20 in WM and 70/30 in GM) than in the fresh counterparts.  
<sup>a</sup>Calculated only over H<sub>2</sub>O samples.

underlying data. Also the S-component amplitude maps exhibit some WM/GM contrast, but these maps are generally more uniform and harder to interpret than those of the U-component. The component amplitude maps are of highest quality for the D<sub>2</sub>O samples but exhibit acceptable quality also for the H<sub>2</sub>O samples.

## 4 | DISCUSSION

In this work, MRI signals from non-pathological human brain samples were observed using ultrashort-T<sub>2</sub> methods and analyzed by decomposition into one aqueous and two

non-aqueous components. The properties of these signal components were investigated for tissue subjected to different experimental procedures, specifically frozen storage and D<sub>2</sub>O exchange for reduction of background water signals. Signal analysis was performed separately for WM and GM, enabling comparison of the two tissue types and establishing a baseline for similar studies in diseased tissue.

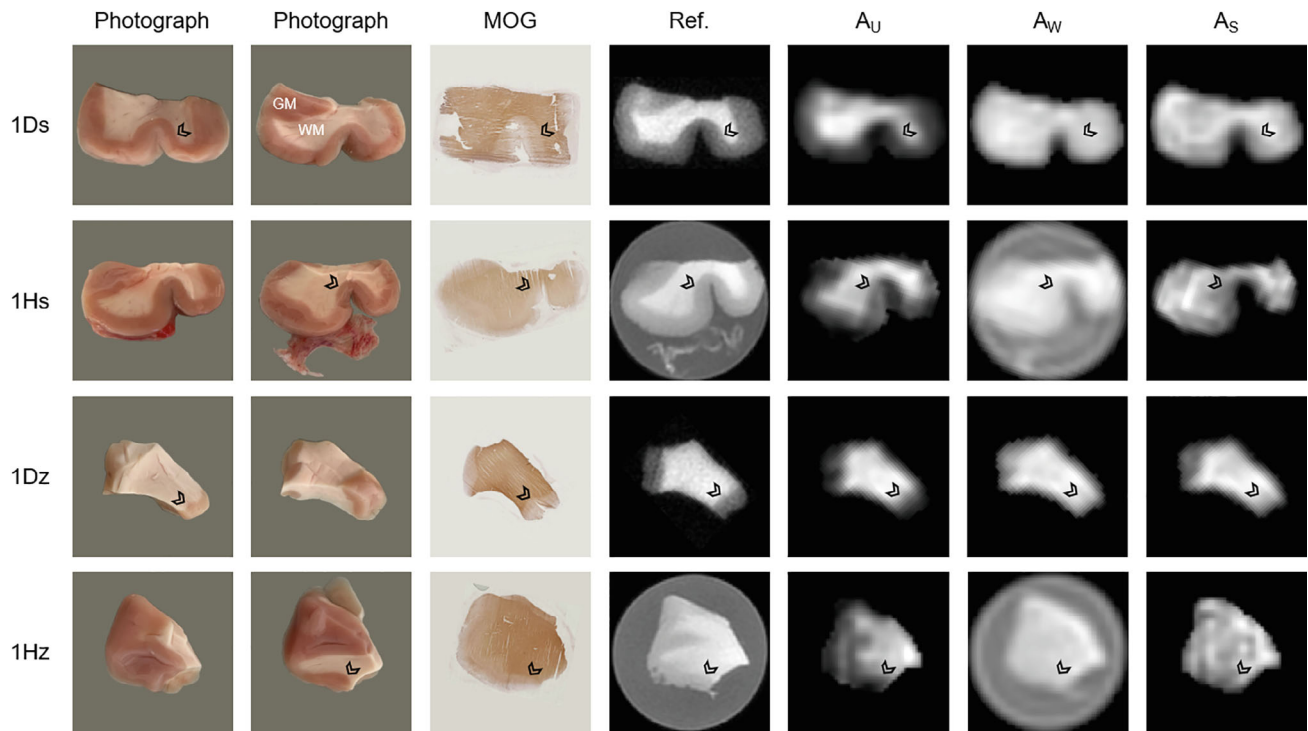
### 4.1 | Sample selection, storage, and preparation

Table 4 gives an overview of myelin bilayer signal components reported in literature. The components reported for *ex vivo* animal tissue are similar to those found in the present study for human tissue, with super-Lorentzian analysis consistently placing the largest non-aqueous signal component at T<sub>2,min</sub> of 5–10 μs and lipid range chemical shift. Additional components, where reported, also correspond well between animal and human tissue.

Freezing tissue had little effect on the parameters of the signal components, as evidenced by Table 2, in which there is greater variation between the two different regions of the brain (tissue blocks 1 and 2) than between fresh and frozen samples. However, for frozen samples, there were some differences in apparent water level and the amplitude relationship of the two non-aqueous components, primarily for H<sub>2</sub>O samples (see Figure 2 and Table 3). A likely explanation for these differences is that freezing affects water content and T<sub>1</sub> by altering the microstructural integrity of the tissue, which together with magnetisation transfer effects influences the component amplitudes.<sup>36</sup>

D<sub>2</sub>O exchange is a useful procedure when attempting to characterize the non-aqueous signal components because it largely removes the otherwise dominant signal contribution of mobile water. The procedure also diminishes any magnetisation transfer effects that can impact the evaluation of component amplitudes and, consequently, decay constants. In addition, the contributions of the non-aqueous signals to the overall phase evolution are difficult to distinguish without D<sub>2</sub>O exchange (see Figure 2), which can lead to unreasonable chemical shift estimates and generally destabilize the fitting procedure. Employing open fits in H<sub>2</sub>O samples led to unstable fit behavior due to the accumulation of effects related to the considerable presence of water, and such fits were therefore not presented in this work.

We showed in Figures 4 and 5 that fixed fits provide acceptable component amplitude map quality also in H<sub>2</sub>O samples, removing the need for D<sub>2</sub>O exchange in cases in which the components of the signal model are known or can be reasonably assumed. This result has important



**FIGURE 4** Comparison of (from left to right) photographs from both sides of the sample, tissue sections stained by myelin oligodendrocyte glycoprotein (MOG) immunohistochemistry, high-resolution ultrashort-T<sub>2</sub> reference images, and fitted component amplitude maps for each sample from tissue block 1 (ordered according to Figure 1). Overall, good correspondence in terms of sample geometry and WM/GM boundaries (see arrowheads at comparable locations) is achieved for all image types. The component amplitude maps show the highest quality for D<sub>2</sub>O samples, although the map quality for H<sub>2</sub>O samples is also considered acceptable

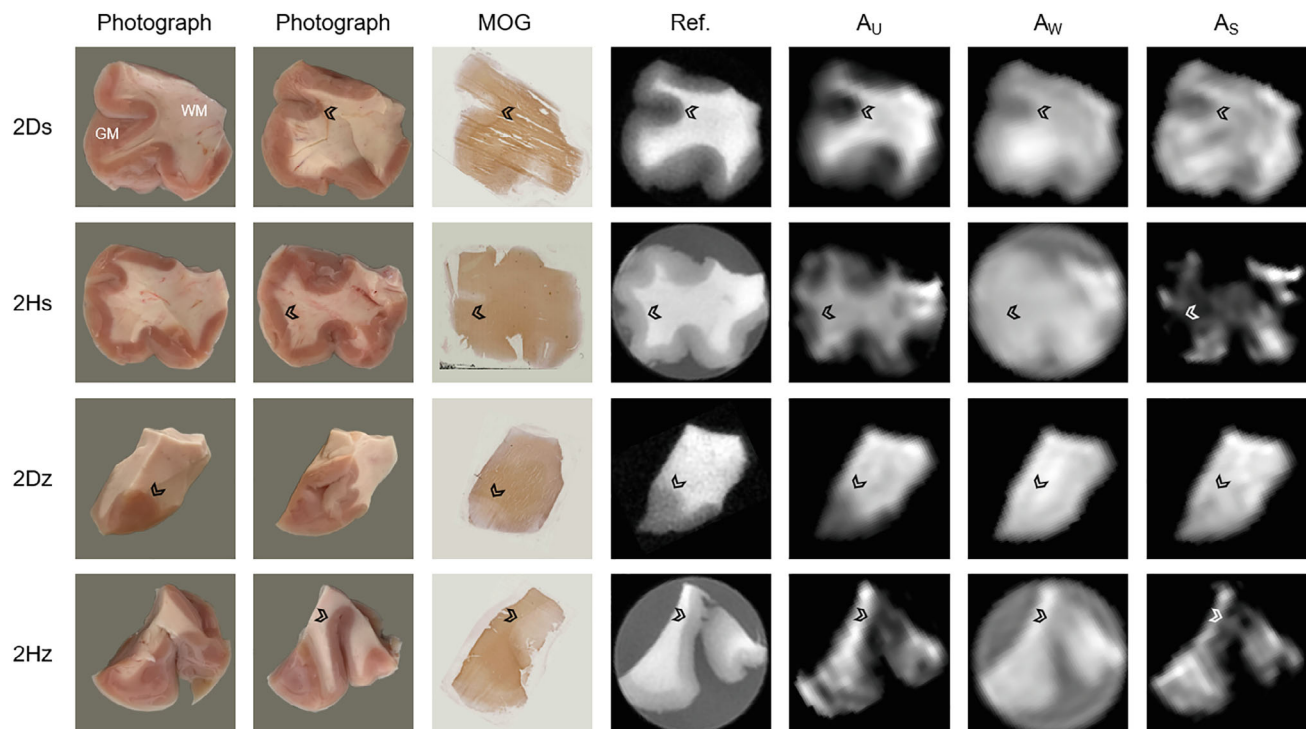


**FIGURE 5** Identical results as presented in Figure 4 but for the samples in tissue block 2. Good correspondence between image types is seen also for these samples, and the component amplitude maps are of the same quality as those presented for the samples from tissue block 1 (see Figure 4). These results further verify the performance of the component amplitude mapping procedure, particularly considering the brain-region dependence of the signal components seen in Table 2

TABLE 4 Overview of reported myelin bilayer signal components (*ex vivo*)

Origin	Sample	Lineshape model	Component values	Component description	Reference
Human	Brain WM	Super-Lorentzian	$T_{2,\min,U} = 5.48 \mu\text{s}$ $T_{2,\min,S} = 102 \mu\text{s}$ $\delta_U = 1.07 \text{ ppm}$ $\delta_S = 2.09 \text{ ppm}$	U: Myelin S: Residual non-aqueous content	Current study
Porcine	Brain WM	Super-Lorentzian	$T_{2,\min,U} = 7.5 \mu\text{s}$ $T_{2,\min,S} = 101 \mu\text{s}$ $\delta_U = 1.38 \text{ ppm}$ $\delta_S = 1.91 \text{ ppm}$	U: Myelin S: Residual non-aqueous content	Weiger et al. <sup>13</sup>
Bovine	Myelin lipid extract	Super-Lorentzian	$T_{2,\min} = 8 \mu\text{s}$ $\delta = 1.5 \text{ ppm}$	Methylene, shortest and largest (74% of total myelin signal)	Wilhelm et al. <sup>12</sup>
Ovine	Cervical spinal cord	Super-Lorentzian	$T_{2,\min} = 10 \mu\text{s}$	Methylene frequency, shortest and largest	Seifert et al. <sup>21</sup>
Bovine	Brain WM	Super-Lorentzian (Gaussian-based)	$\sigma_{\min,U} = 7.2 \mu\text{s}$ $\sigma_{\min,S} = 87 \mu\text{s}$ $\delta_U = \delta_S = 1.3 \text{ ppm}$	U: Shortest and largest S: Remaining	Manning et al. <sup>27</sup>
Rat	Optic nerve	Lorentzian	$T_2 = 80 \mu\text{s}$	Shortest and largest	Horch et al. <sup>26</sup>

Note: Lorentzian-based super-Lorentzian components are characterized (in the time-domain) by decay constant  $T_{2,\min}$ , while Gaussian-based super-Lorentzian components are characterized (in the time-domain) by the SD of the narrowest (i.e., shortest) constituent Gaussian,  $\sigma_{\min}$ . In studies in which multiple values were provided for the same parameter, the mean value is given.  $\delta$  denotes the component chemical shift, which was calibrated with water at 4.7 ppm.

implications for the applicability of the myelin mapping procedure to *in vivo* experiments with acquired data of similar information content, assuming that the underlying signal components *in vivo* are comparable to those found *ex vivo* (it is considered unlikely that biochemical changes directly post-mortem should have a significant effect on signal components given the insignificance of changes introduced by the relatively aggressive procedure of frozen tissue storage).

## 4.2 | Data analysis procedure

Data analysis was performed through a combination of two fitting approaches, namely open and fixed fits, in order to circumvent the inherent limitations of each approach. These limitations have important consequences regarding the interpretation and validity of the fitting results (especially for open fits) and are therefore discussed here in detail.

Open fits can provide valuable information about the parameters of the signal model but are prone to unstable behavior due to their many free parameters as well as interdependencies between the parameters. The instabilities can be explained separately for the magnitude and phase of the signal.

For the magnitude behavior, consider the relationship between component amplitude and decay constant in the case of only one signal component. Because  $TE_1 > 0$ , the component amplitude is unbounded, and the signal magnitude at  $TE_1$  can be reached either with a smaller

decay constant and a larger amplitude or with a larger decay constant and a smaller amplitude –that is, there is no unique solution. Naturally, the fitting process considers the data points at all TEs when determining the optimal parameter set, but component amplitudes and decay constants are still strongly dependent on each other, which corresponds to poor conditioning. With data subject to errors, it is therefore not instructive to compare component amplitudes (e.g., in different tissue types) unless the decay constants of the components are fixed; this caution also extends to comparisons with amplitudes expected from literature.

For the phase behavior, the explanation is more subtle. The component parameter governing the phase evolution is the chemical shift, which manifests as a linear change over time. At low TE for which the non-aqueous components contribute significantly to the acquired signals, the chemical shifts have not had much time to influence the signal phase. Additionally, lower-TE data points have lower SNR because the acquisition duration is shorter. Together, these effects may result in unstable chemical shift estimates, and even minor changes in the acquisition, reconstruction and analysis pipeline can influence the fitted chemical shifts. That said, using the same pipeline for multiple datasets often yielded similar chemical shift results, with values consistently within a reasonable range for primarily lipid signals.

Fixed fits, on the other hand, are comparatively stable and enable component amplitude comparisons, but impose assumptions on the signal components and, consequently, can bias the fitting results. It is therefore

important that component characterization is performed with due care, which relates back to the informed use of open fits (or critical assessment of relevant literature results).

### 4.3 | Component interpretation

The assignment of the fitted U-component to myelin is based on a number of assumptions concerning the size and distinctiveness of the contribution to the rapidly decaying signals by myelin constituents, the validity of the approximations in the signal model, and the ability of the fitting procedure to correctly allocate signal properties to model parameters. As discussed by Weiger et al.,<sup>13</sup> there are strong indications that WM ultrashort- $T_2$  signals indeed largely reflect myelin and that the U-component primarily represents myelin lipids. In the present study, we have further validated the signal model and explored the limitations of the fitting procedure. Overall, we believe that the U-component amplitude is the most quantitative direct measure of WM myelin bilayer content available with current MRI technology.

The situation for GM is fundamentally different because neuronal components such as somata and axons/dendrites (and, hence, non-myelin plasma membranes) constitute a large portion of non-aqueous material and quite likely exhibit similar signal characteristics as the myelin bilayer. Therefore, we cannot claim myelin specificity of the U-component in GM, but contributions from the myelin bilayer to GM signals should nevertheless get assigned to the U-component. It is therefore still likely that changes in myelin are partly reflected in the U-component also for GM.

### 4.4 | Signal components

GM exhibits different component parameters than WM (see Table 2), which likely reflects the different composition of the two tissue types. However, as demonstrated in Figures 4 and 5, fixing fit components based on WM values produced reasonable component amplitude maps also in GM, thus bypassing the need for pre-analysis tissue segmentation. It is worth noting that the signal model was designed based on expected WM behavior, yet it appears to sufficiently represent also GM signals (see Figure 3D).

Considering the full spectrum of decay constants and chemical shifts presented in Table 2 together with the quality of component amplitude maps and region fits displayed in Figures 2, 4 and 5 based simply on fixed fits using average parameter values, we conclude that the exact values of

the component parameters are not of great consequence as long as they are representative of the signal behavior. However, it is important to keep in mind that, for component amplitudes to be comparable, the same fixed values must be used across all analyses.

Although previous studies have reported multiple super-Lorentzian myelin bilayer components,<sup>12</sup> it was not considered necessary here to resolve the rapidly decaying signals into more than two components due to the general similarity and lopsided amplitude distribution of the previously reported components. Nevertheless, signal models with more than three components were briefly explored but did not perform well, as expected for high-dimensional multi-exponential analysis.

### 4.5 | Imaging protocols

The SPI protocol is limited by the minimum TE, which in turn is limited by image resolution and available gradient strength. The minimum TE of 33  $\mu\text{s}$  raises a potential concern regarding the reliability of characterizing the U-component, with  $T_{2,\text{min}}$  of 5.5  $\mu\text{s}$ , from the SPI data presented in this study; this concern ultimately relates to the SNR of the data used for fitting. Signals from a super-Lorentzian component exhibit a  $T_2$  distribution for which  $T_{2,\text{min}}$  describes the shortest-lived signals; consequently, all other signals from the component exhibit  $T_2 > T_{2,\text{min}}$ . For the case of the U-component, 20% of the total signal amplitude remains at  $TE_{\text{min}}$ , and, as can be seen in Figure 2, this signal level is significantly higher than the noise level. It is therefore reasonable to conclude that the U-component can be characterized using the captured signals. This conclusion is supported by the reliability of the signal analysis procedure (demonstrated in Figure 3) and the good correspondence of the presented fitting results to those reported in literature (see Table 4).

The HYFI reference images provide high-resolution depiction of ultrashort- $T_2$  signals, and reflect the contrast seen in the U-component amplitude maps. This raises the question of whether the HYFI images are a sufficient representation of myelin content, which would bypass the resolution limitations of the SPI protocol and its associated signal analysis.

The most pressing argument against relying on single HYFI images concerns myelin specificity. The HYFI images depict the sum of all signal components, and while there are ways to attenuate the contribution of the water component, e.g., by long-TE image subtraction or inversion recovery preparation,<sup>18,37</sup> the signals from the myelin bilayer cannot be separated from other non-aqueous signals. In short, the SPI series facilitates greater myelin



specificity at the cost of image resolution and SNR efficiency. We believe that the insights presented in this study will provide valuable information regarding how best to maintain myelin specificity when transitioning to *in vivo* application, for which the scan limitations are strict.

## 5 | CONCLUSIONS

One aim of the present study was to explore the effects of different experimental procedures on the analysis of myelin bilayer signals, specifically regarding the selection, storage and preparation of imaging samples.

The human brain samples studied in this work exhibited similar component parameters to various animal samples reported in literature. These findings validate the use of animal tissue as a substitute for human tissue, although human tissue still offers obvious advantages depending on the particular purpose of the study.

Furthermore, it was demonstrated that tissue stored in a frozen state is qualitatively equivalent to fresh tissue, but quantitative comparison—in particular of signal amplitudes – between fresh and frozen tissue is limited.

Lastly, D<sub>2</sub>O exchange, which has been a popular method to reduce background water signals in previous short-T<sub>2</sub> myelin studies, was found also here to provide benefits for signal component investigation. However, when working with a fixed signal model, D<sub>2</sub>O exchange was not necessary to achieve acceptable myelin maps.

Another aim of this study was to investigate the rapidly decaying MRI signals from non-pathological human brain. We showed that WM and GM can be described by the same signal model, which consists of two non-aqueous components with super-Lorentzian lineshape (T<sub>2,min</sub>s of around 5–10 μs and 100–200 μs, and chemical shifts in the lipid range) and one aqueous component with Lorentzian lineshape.

The employed myelin mapping procedure exhibited stable behavior, and the myelin maps corresponded well to sample anatomy and MOG staining density. The procedure can therefore be recommended for future use (contingent on the data being of comparable quality and structure to those presented in this study) and can be used without extensive prior signal analysis by fixing component parameter values reported here.

Overall, the results obtained in this work can act as a foundation for signal interpretation in further *ex vivo* and *in vivo* myelin studies.

## ACKNOWLEDGMENTS

The authors thank Karl Frontzek from the Institute of Neuropathology, University Hospital Zurich, Switzerland,

for providing the brain samples, and Richard Reynolds from the UK Multiple Sclerosis Tissue Bank for providing MOG antibody.

## CONFLICT OF INTEREST


Klaas Paul Pruessmann holds a research agreement with and receives research support from Philips and is a shareholder of Gyrotools LLC.

## DATA AVAILABILITY STATEMENT

Example data and MATLAB (MathWorks, USA) analysis code is provided at <https://gitlab.ethz.ch/shortT2mri/myelin-multi-te-fitting>.

## ORCID

Emily Louise Baadsvik  <https://orcid.org/0000-0001-5941-5532>

Romain Froidevaux  <https://orcid.org/0000-0001-7550-5554>

Klaas Paul Pruessmann  <https://orcid.org/0000-0003-0009-8362>

## REFERENCES

- Norton WT, Cammer W. Isolation and characterization of myelin. In: Morell P, ed. *Myelin*. 2nd ed. Springer; 1984:147-195.
- Rasband MN, Macklin WB. Myelin structure and biochemistry. In: Brady ST, Siegel GJ, Albers RW, Price DL, eds. *Basic Neurochemistry*. 8th ed. Elsevier; 2012:180-199.
- Popescu BFG, Lucchinetti CF. Pathology of demyelinating diseases. *Annu Rev Pathol*. 2012;7:185-217.
- Love S. Demyelinating diseases. *J Clin Pathol*. 2006;59:1151-1159.
- Laule C, Vavasour IM, Kolind SH, et al. Magnetic resonance imaging of myelin. *Neurotherapeutics*. 2007;4:460-484.
- Baron W, Hoekstra D. On the biogenesis of myelin membranes: sorting, trafficking and cell polarity. *FEBS Lett*. 2010;584:1760-1770.
- Piredda GF, Hilbert T, Thiran J-P, Kober T. Probing myelin content of the human brain with MRI: a review. *Magn Reson Med*. 2021;85:627-652.
- MacKay AL, Laule C. Magnetic resonance of myelin water: an *in vivo* marker for myelin. *Brain Plast*. 2016;2:71-91.
- Varma G, Duhamel G, de Bazelaire C, Alsop DC. Magnetization transfer from inhomogeneously broadened lines: a potential marker for myelin. *Magn Reson Med*. 2015;73:614-622.
- Laule C, Moore GRW. Myelin water imaging to detect demyelination and remyelination and its validation in pathology. *Brain Pathol*. 2018;28:750-764.
- Heath F, Hurley SA, Johansen-Berg H, Sampaio-Baptista C. Advances in noninvasive myelin imaging. *Dev Neurobiol*. 2018;78:136-151.
- Wilhelm MJ, Ong HH, Wehrli SL, et al. Direct magnetic resonance detection of myelin and prospects for quantitative imaging of myelin density. *Proc Natl Acad Sci*. 2012;109:9605-9610.



13. Weiger M, Froidevaux R, Baadsvik EL, Brunner DO, Rösler MB, Pruessmann KP. Advances in MRI of the myelin bilayer. *Neuroimage*. 2020;217:116888.
14. Weiger M, Pruessmann KP. Short- $T_2$  MRI: principles and recent advances. *Prog Nucl Magn Reson Spectrosc*. 2019;114-115:237-270.
15. Froidevaux R, Weiger M, Rösler MB, et al. High-resolution short- $T_2$  MRI using a high-performance gradient. *Magn Reson Med*. 2020;84:1933-1946.
16. Du J, Ma G, Li S, et al. Ultrashort echo time (UTE) magnetic resonance imaging of the short  $T_2$  components in white matter of the brain using a clinical 3T scanner. *Neuroimage*. 2014;87:32-41.
17. Nayak KS, Pauly JM, Gold GE, Nishimura DG. Imaging Ultra-Short  $T_2$  Species in the Brain. *Proceedings of the ISMRM 8th Scientific Meeting & Exhibition*. International Society for Magnetic Resonance in Medicine; 2000:509.
18. Waldman A, Rees J, Brock C, Robson M, Gatehouse P, Bydder G. MRI of the brain with ultra-short echo-time pulse sequences. *Neuroradiology*. 2003;45:887-892.
19. Sheth V, Shao H, Chen J, et al. Magnetic resonance imaging of myelin using ultrashort Echo time (UTE) pulse sequences: phantom, specimen, volunteer and multiple sclerosis patient studies. *Neuroimage*. 2016;136:37-44.
20. Seifert AC, Umphlett M, Hefti M, Fowkes M, Xu J. Formalin tissue fixation biases myelin-sensitive MRI. *Magn Reson Med*. 2019;82:1504-1517.
21. Seifert AC, Li C, Wilhelm MJ, Wehrli SL, Wehrli FW. Towards quantification of myelin by solid-state MRI of the lipid matrix protons. *Neuroimage*. 2017;163:358-367.
22. Fan SJ, Ma Y, Zhu Y, et al. Yet more evidence that myelin protons can be directly imaged with UTE sequences on a clinical 3T scanner: Bicomponent  $T_2^*$  analysis of native and deuterated ovine brain specimens. *Magn Reson Med*. 2018;80:538-547.
23. Fan SJ, Ma Y, Chang EY, Bydder GM, Du J. Inversion recovery ultrashort echo time imaging of ultrashort  $T_2$  tissue components in ovine brain at 3T: a sequential D2O exchange study. *NMR Biomed*. 2017;30:e3767.
24. Boucneau T, Cao P, Tang S, et al. In vivo characterization of brain ultrashort- $T_2$  components. *Magn Reson Med*. 2018;80:726-735.
25. Ercan E, Boernert P, Webb A, Ronen I. Whole-brain tissue-based assessment of the ultrashort  $T_2$  component using 3D UTE MRI Relaxometry. *Proceedings of the ISMRM 20th Annual Meeting & Exhibition*. International Society for Magnetic Resonance in Medicine; 2012:4279.
26. Horch RA, Gore JC, Does MD. Origins of the ultrashort- $T_2$  1H NMR signals in myelinated nerve: a direct measure of myelin content? *Magn Reson Med*. 2011;66:24-31.
27. Manning AP, Mackay AL, Michal CA. Understanding aqueous and non-aqueous proton  $T_1$  relaxation in brain. *J Magn Reson*. 2021;323:106909.
28. Weiger M, Overweg J, Rösler MB, et al. A high-performance gradient insert for rapid and short- $T_2$  imaging at full duty cycle. *Magn Reson Med*. 2018;79:3256-3266.
29. Weiger M, Brunner DO, Dietrich BE, Müller CF, Pruessmann KP. ZTE Imaging in Humans. *Magn Reson Med*. 2013;70:328-332.
30. Brunner DO, Furrer L, Weiger M, et al. Symmetrically biased T/R switches for NMR and MRI with microsecond dead time. *J Magn Reson*. 2016;263:147-155.
31. Balcom BJ, MacGregor RP, Beyea SD, Green DP, Armstrong RL, Bremner TW. Single-point ramped imaging with  $T_1$  enhancement (SPRITE). *J Magn Reson Ser A*. 1996;123:131-134.
32. Froidevaux R, Weiger M, Rösler MB, Brunner DO, Pruessmann KP. HYFI: hybrid filling of the dead-time gap for faster zero echo time imaging. *NMR Biomed*. 2021;34:e4493.
33. Wennerström H. Proton nuclear magnetic resonance lineshapes in lamellar liquid crystals. *Chem Phys Lett*. 1973;18:41-44.
34. Bloom M, Burnell EE, Valic MI, Weeks G. Nuclear magnetic resonance line shapes in lipid bi-layer model membranes. *Chem Phys Lipids*. 1975;14:107-112.
35. Van der Knaap MS, Valk J. Myelin and white matter. *Magnetic Resonance of Myelination and Myelin Disorders*. Springer Science & Business Media; 2005.
36. Evans SD, Nott KP, Kshirsagar AA, Hall LD. The effect of freezing and thawing on the magnetic resonance imaging parameters of water in beef, lamb and pork meat. *Int J Food Sci Technol*. 1998;33:317-328.
37. Gatehouse P, Bydder G. Magnetic resonance imaging of short  $T_2$  components in tissue. *Clin Radiol*. 2003;58:1-19.

## SUPPORTING INFORMATION

Additional supporting information may be found in the online version of the article at the publisher's website.

**Appendix S1:** Part 1: Decay functions in the signal model  
Part 2: Immunohistochemistry procedure  
Part 3: Demonstration of  $T_1$  weighting

**How to cite this article:** Baadsvik EL, Weiger M, Froidevaux R, Faigle W, Ineichen BV, Pruessmann KP. Mapping the myelin bilayer with short- $T_2$  MRI: Methods validation and reference data for healthy human brain. *Magn Reson Med*. 2023;89:665-677. doi: 10.1002/mrm.29481